

Evidence of a rutile-phase characteristic peak in low-energy loss spectra

M. Launay, F. Boucher, and P. Moreau

Institut des Matériaux Jean Rouxel, UMR6502 CNRS–Université de Nantes, Laboratoire de Chimie des Solides, 2 Rue de la Houssinière, Boîte Postale 32229, 44322 Nantes Cedex 3, France

(Received 18 July 2003; published 7 January 2004)

Low-energy loss spectra (LELS) from electron energy loss spectroscopy (EELS) in a transmission electron microscope do not yield structural information as readily as do core loss spectra. In order to make LELS a more general technique, we have studied the 10–15 eV energy range in some MO_2 compounds in great detail and identified a characteristic peak of a specific structural unit. A comparison of experimental EELS spectra and *ab initio* density-functional theory calculations (WIEN2K code) is presented. A definite peak around 14 eV appears in the imaginary part of the dielectric functions of those structures containing rutile units. These rutile units are M_3O_{15} clusters made of edge- and corner-sharing octahedra, which when stacked lead to rutile structures, among others. The peak is present in rutile phases with $M = \text{Ti, V, Cr, Mn, Si, Ge, Sn, and Pb}$. Other structures, such as Ramsdellite or high-pressure TiO_2 phases, also contain the necessary structural unit and indeed present the same feature. The origin of the peak can be elucidated by means of band structure calculations and an analysis of the orbitals involved in the transition. The existence of such a peak, always visible around 14 eV whatever M , shows its remarkable universality.

DOI: 10.1103/PhysRevB.69.035101

PACS number(s): 79.20.Uv, 82.80.Pv, 77.22.Ch, 71.20.Be

I. INTRODUCTION

Improving our knowledge of materials on a nanometer scale is becoming increasingly important to scientific exploration. Miniaturization, interface issues, and composite materials can only be understood by way of precise information about the local atomic and electronic structures. In this context, electron energy loss spectroscopy (EELS) in a transmission electron microscope (TEM) is of special interest. The spatial resolution of the EELS technique is, in most cases, better than 1 nm, and the energy resolution is usually better than 1 eV. As high-resolution electron microscopy can be performed at the same time on the same area and leads to images with a 2 Å point to point resolution, EELS in a TEM meets the criteria for being one of the most extensively used techniques in nanomaterial research. The nonrelativistic theory for isotropic bulk materials, whatever the energy loss, indicates that the spectrum is proportional to $\text{Im}[-1/\varepsilon(E)]$, with $\varepsilon(E)$ being the complex dielectric function of the material. For large energy loss values, the imaginary part of the dielectric function ε_2 is very small whereas its real part ε_1 tends toward 1. So, for high energy losses, the spectrum is proportional to ε_2 , while the full formula has to be used for low losses. EELS is consequently often separated into two parts: the core loss region (above 100 eV electron energy loss approximately) and the low-loss region (between 0 and 100 eV). The core loss community would tend to collaborate with the x-ray absorption spectroscopy one owing to the very similar electron processes involved (proportional to ε_2). The low-loss one would rather compare results with optical experiments since the complete dielectric function is their common language. In both, “fingerprint” studies are often used, allowing the identification of phases by comparison with well-known spectra. Extraction of more general information from the spectra is more cumbersome. In high losses, extended energy loss fine structures (EXELFS) experiments can be very useful to obtain the radial distribution of surrounding atoms.¹ The precise recording of the first 10 eV of

the spectra (ELNES, energy loss near edge structures) can give information not only about the oxidation state via the L_2/L_3 ratio,² and the absolute energy position,³ but also about local symmetry via d level splittings in transition metal elements,⁴ and orbital hybridization.^{5,6}

In low losses, available tools are less numerous and not as widely used. Plasmon peak analysis (essentially positions) can give useful information on the nature of the interface⁷ and bulk properties.^{8,9} The existence of a π plasmon peak is, for example, an indication of the low-dimensional character of a material. Direct and indirect gap determination is also possible via a careful analysis of the shape of the intensity onset.^{10,11} Compared to core losses, this may appear as a relative lack of general information that one could easily extract from low energy loss spectra (LELS). Also, LELS originate from all possible transitions between the valence band and the conduction band. Thus, the valence band being made up of dispersed levels as opposed to almost flat core levels, the interpretation of LELS is *a priori* more difficult. Finally, LELS usually have a delocalized nature which prevents them from giving atomic resolution information. All this might explain why this region is greatly neglected compared to the high-loss one.

Nevertheless, on the localization issue, the intensity mainly results from interaction with the material over a few nanometers, and by using off-axis detectors the signal becomes almost as localized as the core loss one.¹² Furthermore, a remarkable advantage of LELS over ELNES/EXELFS consists of a much lower acquisition time. In the context of beam-sensitive or fast-evolving materials, tenth-of-a-second measurements increase the range of possible analysis when compared with the seconds or tens of seconds necessary for core loss acquisitions. Finally, we believe that, thanks to the discovery of characteristic peaks, such as the one described hereafter, future experiments will reveal other such peaks in other materials, leading to more extensive use of LELS.

Titanium dioxides are of special interest for their various

potential (or already effective) uses as high- k gate insulators,¹³ as paint pigments,¹⁴ in photocatalysis for decomposition of contaminants,¹⁵ in photovoltaic cells,¹⁶ as negative electrode materials for lithium batteries,¹⁷ as multilayers for quantum wells,¹⁸ and as optical photonic crystals.¹⁹ These applications involve nanostructured materials, demonstrating the need for techniques that are able to determine dioxide phase structures on a nanometer scale. Theoretical band structure calculations on TiO₂ compounds are numerous,^{20–24} but usually focus either on band gap and bonding issues or on the overall shape of the simulated LELS spectra. A more detailed study of the 10–20 eV energy range needed to be performed.

We found that a peak in the low-loss region (around 14 eV) is characteristic of a special arrangement of octahedra. This applies not only to titanium dioxides but also to other compounds such as other transition metal dioxides and dioxides of 14th group elements. This is, to our knowledge, the first example of this kind of general rule in the low-loss region.

In this paper, we first of all describe the experimental and calculation details used to reveal this characteristic peak; then we analyze its origin by means of a careful study of the TiO₂ rutile band structure. Other TiO₂ phases allow us to pinpoint the structural unit responsible for the transition and, finally, we generalize this discussion to other MO₂ rutile phases with M belonging to either the first row of transition metals or the 14th column.

II. EXPERIMENTAL DETAILS

The powders were crushed in acetone and deposited onto holey carbon grids. Prior to its introduction into the electron microscope, the sample holder loaded with the sample was vacuum evacuated at 100 °C to remove any contamination. The Hitachi HF2000 transmission electron microscope, equipped with a field emission gun and a GATAN PEELS 666 spectrometer, was operated at 100 kV. The energy resolution, measured as the full width at half maximum of the zero loss peak (ZLP), was 0.75 eV and the energy dispersion was set to 0.05 eV/channel. Total acquisition time was 3 s to optimize signal to noise ratio but 0.2 s acquisitions already showed excellent quality. All spectra were first gain and dark count corrected and then deconvoluted by the ZLP recorded in a hole of the grid, using the PEELS program.²⁵ Next, the single scattering spectra were obtained following Stephen's procedure,²⁶ which also gave the ratio t/λ (t the thickness of the analyzed crystal and λ the inelastic mean free path). In order to get the sample's thickness, we estimated λ using the following formula:¹² λ (nm) = $106F(E_0/E_m)/\ln(2\beta E_0/E_m)$ with β in mrad, E_0 in keV, and E_m in eV. F is a relativistic factor equal to 0.768 for $E_0 = 100$ keV and the mean energy loss E_m can be estimated as $E_m = 7.6Z_{\text{eff}}^{0.36}$. The effective atomic number Z_{eff} is defined as $Z_{\text{eff}} = \sum_i f_i Z_i^{1.3} / \sum_i f_i Z_i^{0.3}$ where f_i is the atomic fraction of each element of atomic number Z_i . In the case of TiO₂, $Z_{\text{eff}} = 13.7$ so that $E_m = 19.5$ eV. Finally, with $\beta = 9$ mrad, we obtain $\lambda = 92$ nm. This value shows a reasonable agreement with published values for other oxides although it might be slightly underestimated.²⁷

The orientation of the crystals was obtained by electron diffraction prior to the spectrum recording. In all cases, the convergent and collection angles were 1.4 mrad and 9 mrad, respectively. In order to obtain intensities as probability/eV units and get an absolute comparison with calculations, the experimental spectrum intensities were divided by the zero loss intensity (between -3 and 2 eV) and the energy dispersion.²⁸

III. CALCULATION DETAILS

All calculations were done using the full potential linearized augmented plane wave program WIEN2K,^{29,30} in the generalized gradient approximation (GGA).³¹ Published experimental atomic structures were used for the calculations of rutile,³² anatase,³³ II,³⁴ bronze,³⁵ and Ramsdellite TiO₂.³⁶ Structural parameters for other rutile compounds with $M = V$,³⁷ Cr,³⁸ Mn,³⁹ Si,⁴⁰ Ge,⁴¹ Sn,⁴² and Pb,⁴³ were obtained from the literature. The muffin-tin radii for M and oxygen atoms were 1.8 and 1.6 a. u., respectively. In the case of SiO₂ these radii were 1.75 and 1.55 a. u. due to the shorter interatomic distances. The cutoff of the plane-wave expansion was given by $R_{\text{MT}} \times K_{\text{max}} = 7$. Depending on the size of the Brillouin zone for the considered phases (phases with $Z = 2$ or $Z = 4$), either 4500 total \mathbf{k} points (430 irreducible) or 2250 total \mathbf{k} points (300 irreducible) were used, respectively, to calculate the optical dielectric functions. No significant changes were obtained in varying all these parameters. Eigenvalues were computed up to 60 eV above the Fermi level. Matrix elements from the valence band states ψ_k^v to the conduction band states ψ_k^c were calculated to obtain the imaginary part of the dielectric function given by⁴⁴

$$\begin{aligned} \varepsilon_{2ii} &= \text{Im } \varepsilon_{ii}(\omega) \\ &= \frac{4\pi^2 e^2}{m^2 \omega^2 V} \sum_{v,c,k} |\langle \psi_k^v | \mathbf{p}_i | \psi_k^c \rangle|^2 \times \delta(E_{\psi_k^c} - E_{\psi_k^v} - \hbar\omega), \end{aligned}$$

where $E_{\psi_k^c}$ and $E_{\psi_k^v}$ are the quasiparticle energies (approximated to the GGA eigenvalues), V is the volume of the unit cell, and \mathbf{p}_i is the momentum operator with $i = x, y, \text{ or } z$. In this paper, orthogonal lattices are considered, so that only the diagonal components of the dielectric tensor are pertinent (ε_{2xx} , ε_{2yy} and ε_{2zz}), with the $x, y, \text{ and } z$ directions corresponding to the crystal Cartesian axes. The real parts of the dielectric functions calculated (ε_{1xx} , ε_{1yy} , and ε_{1zz}) were obtained via a Kramers-Krönig (KK) analysis.

As expected with the use of density-functional theory (DFT) methods, band gaps were calculated to be smaller than experimentally observed. In the case of rutile and anatase TiO₂ (Figs. 1 and 2), and to give a closer agreement with experiments, a "scissors operator" was introduced to shift the dielectric functions upward. All other calculations were left unshifted. In order to obtain simulated spectra as probability/eV, a relativistic formula taking into account the thickness, scattering conditions, and anisotropy of uniaxial materials was used.^{45,46} Finally, these theoretical spectra

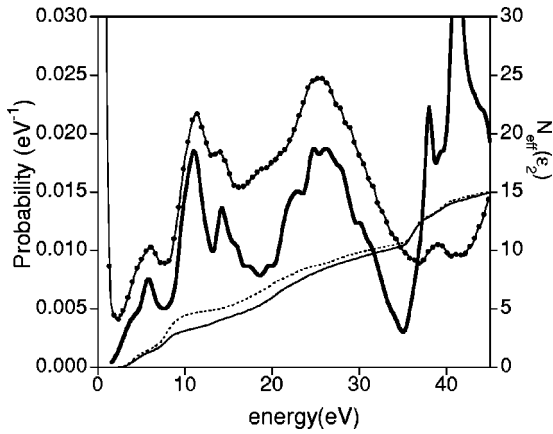


FIG. 1. Experimental and theoretical low-energy loss spectra for rutile TiO_2 as well as theoretical effective number of electrons contributing to the spectrum. The experimental conditions $\alpha = 1.4$ mrad, $\beta = 9$ mrad, and $\gamma = 0^\circ$ (angle between the c axis and the optical axis of the microscope) were used in the relativistic calculation of the spectrum. The Bethe sum rule based on ϵ_2 was used to calculate N_{eff} . Thin line with filled circles: experimental spectrum; thick line: calculated spectrum. Thin line: N_{eff} based on ϵ_{2xx} ; dotted line: N_{eff} based on ϵ_{2zz} .

were convoluted by a Gaussian function (full width at half maximum = 0.75 eV) to account for the limited resolution of the experiment.

We would like to mention that a frequently used method of comparing experimental and theoretical results consists in retrieving the dielectric functions from the measured spectra via a KK analysis,¹² and in confronting them with the *ab initio* dielectric functions. This KK analysis can be extended to include surface plasmon effects by using self-consistent simulations of the spectra,⁴⁷ or anisotropy effects.⁴⁸ However, in that latter case, the experimental procedure becomes complex and relies on a nonrelativistic approximation. A further extension of this analysis would take into account relativistic effects (the importance of which has previously been

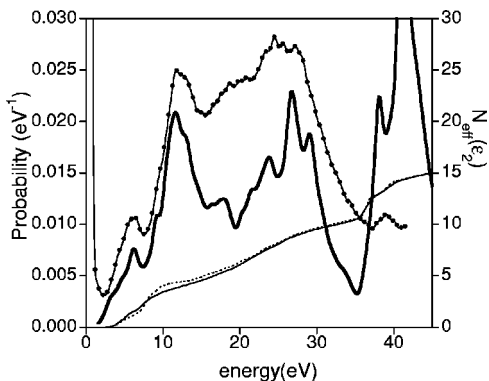


FIG. 2. Experimental and theoretical low-energy loss spectra for anatase TiO_2 as well as theoretical effective number of electrons contributing to the spectrum. The experimental conditions $\alpha = 1.4$ mrad, $\beta = 9$ mrad, and $\gamma = 0^\circ$ were used in the relativistic calculation of the spectrum. The Bethe sum rule based on ϵ_2 was used to calculate N_{eff} . Thin line with filled circles: experimental spectrum; thick line: calculated spectrum. Thin line: N_{eff} based on ϵ_{2xx} ; dotted line: N_{eff} based on ϵ_{2zz} .

shown),⁴⁶ as well as both surface and probe convergence effects, and would lead to extremely complex analytical formulas with an intermixing of ϵ_{xx} and ϵ_{zz} terms and diffusion vector components.^{45,46} The resulting iterative KK analysis would be particularly time consuming. Furthermore, one of the major arguments against the use of KK analyses is that they always require a somewhat arbitrary extrapolation of the low-energy loss signal (below 3 eV) due to the presence of the zero loss peak. Finally, very recently, García de Abajo and Howie developed purely numerical calculations of LELS spectra for any material shape, even the most complex ones.⁴⁹ In the crucial context of nanomaterial studies, this would mean that KK analyses of EELS spectra could become irrelevant. Consequently, we believe the simulation of experimental LELS spectra using *ab initio* dielectric functions to be the most appropriate way of comparison.

IV. RESULTS AND DISCUSSION

A. Comparison of rutile TiO_2 with anatase TiO_2

1. Simulation of experimental spectra

Experimental spectra are presented in Figs. 1 and 2 for both rutile and anatase phases. Theoretical dielectric functions for both phases were used to simulate spectra which take into account the relativistic nature of the electrons ($v = 0.548c$, c the speed of light), the thickness (d) of the samples, the uniaxial structure as well as the convergent and collection angles ($\alpha = 1.4$ and $\beta = 9.0$ mrad). The experimental t/λ values were 0.63 and 0.69 for rutile and anatase, respectively. As $\lambda = 92$ nm, the corresponding thicknesses were $d = 580$ and 635 Å, respectively. For these figures only, a +0.4 eV “scissors operator” was used to match both experimental spectra.

A lack of absolute intensity in the theoretical calculations, when compared to experiments, is observed for both spectra. This reflects insufficient knowledge of the inelastic mean free path and/or deconvolution inexactness and/or uncertainty in the normalization procedure (dividing by I_0 is an approximation).²⁸ Except above 30 eV, the agreement is found to be very strong concerning relative peak intensities as well as energy peak positions (thanks to the 0.4 eV shift). Above 30 eV and in particular for the titanium $M_{2,3}$ edges (around 40 eV), the intensities are calculated to be way too high when compared with experiment. Local field effects are not taken into account in our calculation and, as previously demonstrated by Vast *et al.*,²⁴ they lead to a drastic intensity modification for these edges. However, local field effects or time dependent calculations do not seem to improve the description of the intensity around 20 eV: in both phases, a dent is calculated where a bump is observed experimentally. Calculations with and without these effects were proven to be very similar in the 10–20 eV energy region²⁴ and, for our purpose (the 14 eV peak), they can safely be neglected.

The small intensity in the 5–8 eV region corresponds to transitions from the top of the valence band into the T_{2g} and E_g levels of the titanium d orbitals, in a nearly octahedral potential. In this energy range, hardly any difference can be found between the anatase and rutile phases. The region is

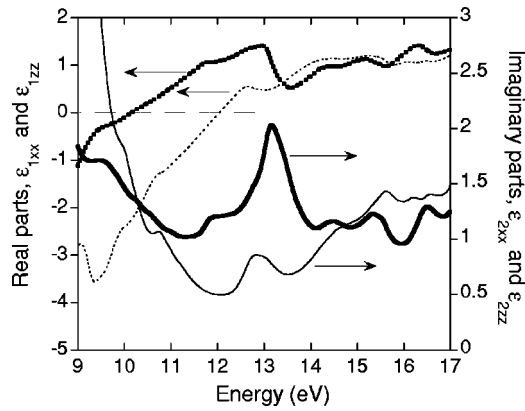


FIG. 3. Calculated real (dotted lines) and imaginary (full lines) parts of the dielectric function for rutile TiO_2 . A zoom is presented on the region of interest for discussion of the 14 eV peak. Both perpendicular ϵ_{2xx} (thick lines) and parallel ϵ_{2zz} orientations to the c axis are shown.

indeed characteristic of the very local symmetry around the titanium atom and, from an initial approximation, all TiO_2 phases are based on various stackings of octahedra. In addition, the initial and final levels involved in the Brillouin zone are too numerous and too dispersed and the EELS resolution too low to produce characteristic spectra such as those obtained in core $L_{2,3}$ titanium edges. As discussed in the following paragraph, it is interesting to notice that this lack of discrimination does not hold for higher-energy peaks (10–20 eV region) where the two phases are clearly distinguishable. This region could be viewed as the equivalent of the multiple scattering region in ELNES. Above 20 eV, the spectra of the two phases are back to a strong resemblance. Consequently, a thorough understanding of the 10–20 eV region is essential to make the low-energy loss spectrum a valuable analytical tool for phase determination.

2. Origin of the 14 eV peak

As already pointed out by other authors,²² a clear distinction between rutile and anatase phases can be seen in the 10–20 eV region. Most notably, whereas a peak is present around 14 eV in the rutile spectrum, it cannot be found in the anatase one.

Considering the strong agreement between theory and experiment, we thought it justified to use calculations to explain the reasons for this extra peak in the rutile phase. By analogy with the Drude and Lorentz models, optical/EELS excitation can be separated into two different natures: a collective one and a single particle one. The first one is characterized, in the real part of the dielectric function, by the upward crossing of the abscissa axis. The second one is characterized by a well-defined peak in the imaginary part of the dielectric function. In Figs. 3 and 4, the calculated real and imaginary parts of the dielectric functions for the rutile and anatase phases are presented. In both cases, ϵ_1 crosses the abscissa axis around 10 eV, which corresponds to the collective excitation of approximately four valence band electrons. This effective number of electrons (N_{eff}) contributing up to a selected energy is calculated using the Bethe

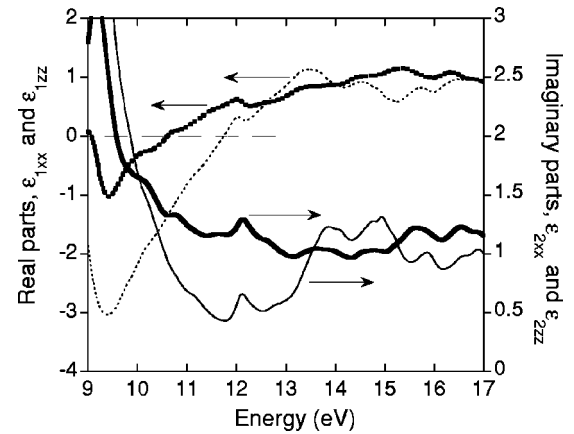


FIG. 4. Calculated real (dotted lines) and imaginary (full lines) parts of the dielectric function for anatase TiO_2 . A zoom is presented on the region of interest for discussion of the 14 eV peak. Both perpendicular ϵ_{2xx} (thick lines) and parallel ϵ_{2zz} orientations to the c axis are shown.

sum rule on the imaginary parts of the dielectric functions.^{12,50} The resulting theoretical curves for both phases are given in Figs. 1 and 2. In the rutile phase, N_{eff} for ϵ_{2zz} is higher than for ϵ_{2xx} , demonstrating that the collective excitation of electrons is larger in the direction parallel to the rutile chains (z) than in the one perpendicular to them (x, y). The value of four electrons is linked to the existence of a nonbonding and a π band in the valence band, as discussed by Sorantin and Schwarz.²⁰ The other 12 σ -bonding electrons originating from the rest of the oxygen $2p$ orbitals, as well as the oxygen $2s$ orbitals, contribute at higher energies. As commonly seen in multielement compounds, the exhaustion of these transitions is not attained before the excitation of the titanium $3p$ electrons, which explains the below $N_{\text{eff}} = 16$ value observed at 35 eV.

Inspection of ϵ_2 , around 13 eV, clearly shows a peak in the rutile phase which is absent in the anatase one. This 13.2 eV peak in ϵ_{2xx} (i.e., in a direction perpendicular to z) corresponds to the 14 eV peak in the spectrum after introduction of the scissors operator. As an electron is excited from the valence band to the conduction band, a so-called interband transition appears. It is that which is responsible for the rutile/anatase spectrum difference.

The bands involved in this particular peak can be found by carefully analyzing the matrix elements for each band combination. For the sake of clarity, only a selection of “valence band i –conduction band j ” transitions is presented in Fig. 5. Around 13 eV, the matrix element is visibly dominant for the band 22–band 35 transition (band numbers counted from the bottom). Finally, by removing the A point ($\frac{1}{2} \frac{1}{2} \frac{1}{2}$) and its close neighbors in the \mathbf{k} point list used to generate the “22 to 35” matrix elements, we show that this A point is responsible for the main intensity of the 13.2 eV peak (Fig. 6). This main transition can be visualized on the band structure as an arrow of which the length is precisely 13.2 eV (Fig. 7). Our band structure is almost identical to the one published and extensively discussed by Sorantin and Schwarz,²⁰ although comparison is limited since they did not study levels situated higher than 8 eV above Fermi level.

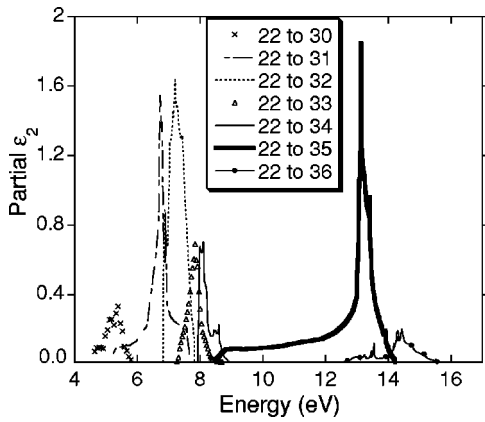


FIG. 5. Selection of band to band transitions in the 4–17 eV region for rutile TiO_2 . The matrix elements at 13.2 eV are clearly dominant for the 22nd to 35th band transition. The large intensity observed in ϵ_{2xx} consequently involves a transition between these two bands.

The character of the 22nd and 35th bands at the A point can be found in Table I. For convenience in the calculation process, values are given in the local coordinate system specific to each atom. In the crystal coordinate system, d_{xy} (Ti) transforms into $d_{x^2-y^2}$ (Ti) and p_y (O) into (p_x, p_y) (O). Subsequently, crystal coordinates will be used for the sake of generality between different structures. In the local D_{4h} symmetry, existing at the A point and in the dipolar approximation, the only authorized transitions are the following: $d_{x^2-y^2}$ (Ti) $\rightarrow p_x, p_y$ (Ti); p_x, p_y (O) $\rightarrow s$ (O) and p_x, p_y (O) $\rightarrow d_{xz}, d_{yz}$ (O). A dipolar transition operator in the x or y direction had to be considered. Indeed, all transitions are forbidden by symmetry in the case of a dipolar transition operator in the z direction, explaining why the 14 eV peak is only observed in ϵ_{2xx} , ϵ_{2yy} , and not in ϵ_{2zz} . The character of the wave function being clearly oxygen rather than titanium in both bands (67% and 11% compared to 7% and 3%, respectively), the p_x, p_y (O) $\rightarrow s$ (O) and p_x, p_y (O) $\rightarrow d_{xz}, d_{yz}$ (O) transitions should prevail (a further confirmation of this attribution will be discussed in the next paragraph). The states involved can be illustrated by an electron density plot corresponding to the two bands (22 and 35) at

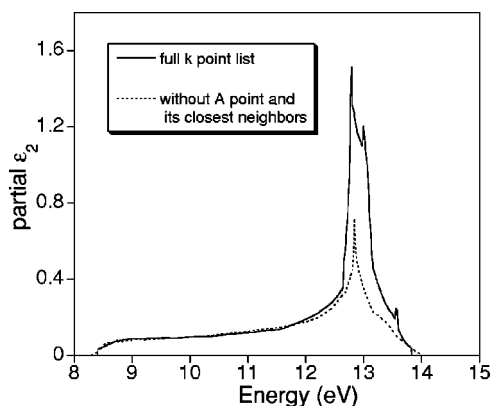


FIG. 6. Matrix elements for the 22nd to 35th band transition for rutile TiO_2 . Full line: all \mathbf{k} points; dotted line: excluding the A point and its nearest neighbors.

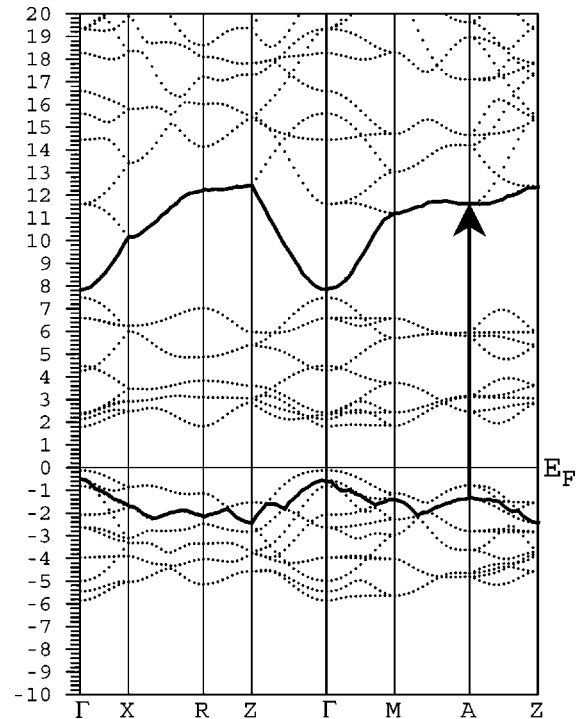


FIG. 7. Band structure of rutile TiO_2 . The transition between the 22nd band and 35th bands at the A point is indicated with an arrow. The two bands are also shown with thicker lines. The energy length of the arrow is precisely 13.2 eV, corresponding to the energy of the peak discussed in this paper.

the A point (Fig. 8). At this \mathbf{k} point, the wave function corresponding to the 22nd band is twofold degenerate, and two independent and symmetry related π -type Ti-O interactions are found in the (110) and $(\bar{1}10)$ directions. As mentioned by Sorantin and Schwarz,²⁰ the rutile structure should be viewed not only as edge-sharing TiO_6 octahedra in the z direction, but also as Ti_3O clusters in a nearly planar configuration. This can be realized in Fig. 8 where the O1, Ti1, Ti2, and Ti3 atoms are labeled. Another view, perpendicular to the c axis, of the octahedra of interest is presented in Fig. 9. These octahedra will be referred to as a Ti_3O_{15} rutile structural unit (RSU) from now on. Molecular orbital considerations show that the existence of such clusters leads to the formation of a Ti-O π -bonding band with a strong O p_y contribution, if the y axis is defined as perpendicular to the Ti_3O plane. This band is involved in our transition of interest.

B. Other TiO_2 phases

Ti_3O_{15} RSUs are not only present in the rutile TiO_2 phase. For this reason, we are now going to examine the 12–15 eV region in other TiO_2 phases. In Fig. 10, the structures under consideration are presented. Calculated imaginary parts of the dielectric functions of the Ramsdellite, II (high-pressure), and bronze phases are shown in Fig. 11. The Ti_3O_{15} RSU, made of two edge-sharing octahedra connected to another octahedron via one of its corners, can be found in the Ramsdellite and II structures as emphasized by the ovals drawn in

TABLE I. Atomic orbital decomposition (l, m) of the wave functions at the \mathbf{k} point involved in the 13–14 eV peak for the rutile, II, and Ramsdellite phases of TiO_2 . All numbers are percentages and refer to the local coordinate system specific to each atom. The total amounts of O and Ti character are also given. Although these quantities should add up to 100%, they do not because the interstitial state values (outside muffin-tin spheres) are not presented. Absent numbers in columns are either null for symmetry reasons or nonrelevant.

	Rutile TiO_2 at the A point (%)				II TiO_2 at the S point (%)				Ramsdellite TiO_2 at the P point (%)					
	Band 22		Band 35		Band 48		Band 71		Band 44			Band 71		
	Ti	O	Ti	O	Ti	O	Ti	O	Ti	O1	O2	Ti	O1	O2
Total	7.2	66.9	2.9	11.2	4.8	72.6	4.1	28.2	9.2	41.3	22.5	4.7	5.6	8.1
s				5.1			2.0	9.1					2.3	1.8
p_x						50.0		7.4		10.5	19.5	0.7		2.4
p_y		66.9	1.7			9.3	0.9	8.2		29.6			0.7	
p_z				2.7		13.1		2.3			2.2		0.7	2.4
d_{z^2}						1.0								
$d_{x^2-y^2}$				1.0	0.7				6.7			0.7		
d_{xy}	7.0			2.2					1.0			1.2		
d_{xz}			1.2											0.6
d_{yz}					1.7		0.5					0.9		

Fig. 10. The dielectric function imaginary parts of these phases present significant peaks in the 13–14 eV range (precisely 13.1 and 13.6 eV, respectively). This is very much like the 13.2 eV peak discussed in the rutile TiO_2 case. The bronze phase does not contain RSUs and its dielectric function does not show a peak in this energy range. A small peak at a lower energy is, however, present: it shows, as expected, that the intensity obtained in the 12–15 eV region is not only due to RSUs. Many transitions can occur and may “fortuitously” appear in this region. Nevertheless, the 1 eV lower energy is a good criterion by which to rule out the presence of RSUs in the bronze phase.

To further demonstrate the RSU involvement in the ϵ_2 of the Ramsdellite and II phases, let us focus on the origin of the peaks considered. The same analysis as the one performed for the rutile phase allows us to identify the bands involved and subsequently the \mathbf{k} points responsible for the main intensity in the 13–14 eV region. This is summarized in Fig. 12 where the particular bands (44 to 71 and 48 to 71 for Ramsdellite and II, respectively) are shown by thick lines

and the main transition is materialized in the form of arrows at the proper \mathbf{k} points. In the II phase, the coordinates of the S \mathbf{k} point for which the matrix elements are large at 13.1 eV are $(\frac{1}{2} \frac{1}{2} 0)$. In the Ramsdellite phase, the P coordinates are $(\frac{1}{2} \frac{1}{4} \frac{1}{2})$.

By drawing the electronic densities corresponding to the 44th band at P for Ramsdellite and to the 48th band at S for the II phase (not shown), we checked that the main contribution is that of oxygen p_y orbitals (if the y axis is chosen perpendicular to the Ti_3O plane), with a small π -type Ti-O interaction. The specific contribution from the oxygen p_y orbitals cannot be easily proven from Table I due to the choice of local rotation matrices. However, in the case of the Ramsdellite phase, the y axis (used to obtain ϵ_2 in Fig. 11) corresponds to the direction defined by two edge-sharing octahedra. In agreement with what has been established for the rutile phase, no contribution is found in ϵ_2 in the y direction (see Ramsdellite’s ϵ_{2yy} in Fig. 11) as it is equivalent to the z direction in the rutile phase (Fig. 10). In the case of the II phase, the directions defined by two edge-sharing octahedra

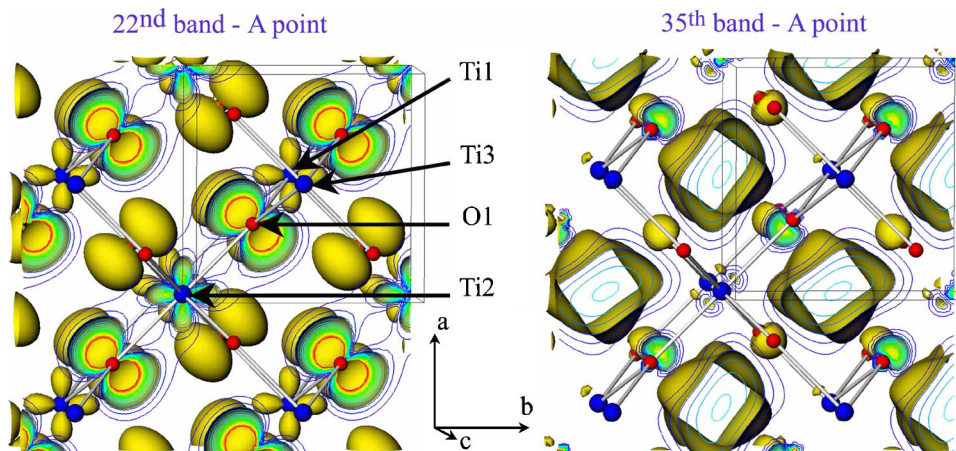


FIG. 8. (Color online) Electron density plots at the A point for both the 22nd band (left) and 35th band (right). In order to make the rutile structural unit and the interaction between p and d orbitals more evident, four unit cells are presented.

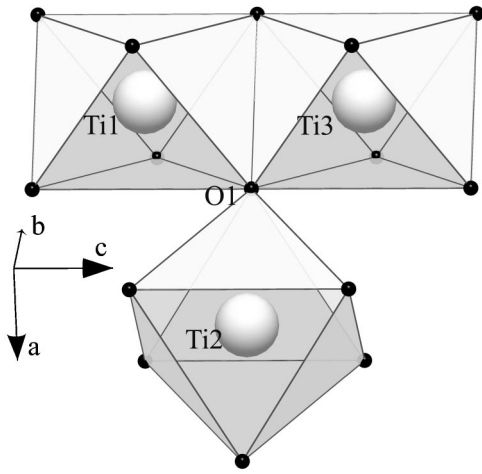


FIG. 9. The Ti_3O_{15} rutile structural unit. Ti1 and Ti3 are at the center of edge-sharing octahedra in the c axis direction, while the other octahedron (Ti2) shares one of its apical oxygen atoms (O1) with them. White spheres: titanium atoms. Black spheres: oxygen atoms.

do not correspond to one of the Cartesian axes. Consequently, none of the ϵ_{2xx} , ϵ_{2yy} , ϵ_{2zz} present a total absence of intensity around 13 eV. Octahedron distortions (especially in the II phase) and lower local symmetry also explain the less pronounced 13.1–13.6 eV peaks in these phases compared to the rutile one.

By comparing all allowed transitions at the A , S , and P k points in the rutile, II, and Ramsdellite phases, we realize that the only common allowed transition is from oxygen p_y orbitals (y axis perpendicular to the Ti_3O plane) to oxygen s orbitals. This conclusively attributes the transition to special oxygen dominant states in the valence and conduction bands.

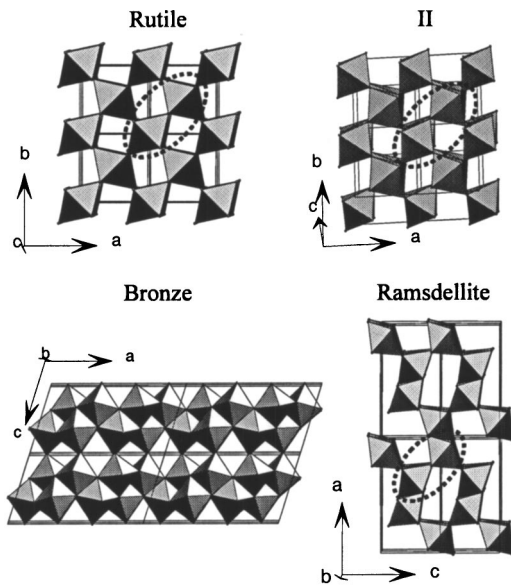


FIG. 10. Representations of rutile, II, Ramsdellite, and bronze TiO_2 structures. The dotted oval identifies, when present, the structural unit responsible for the existence of the electron density presented in Fig. 8. For clarity, some octahedra have been omitted in the II structure.

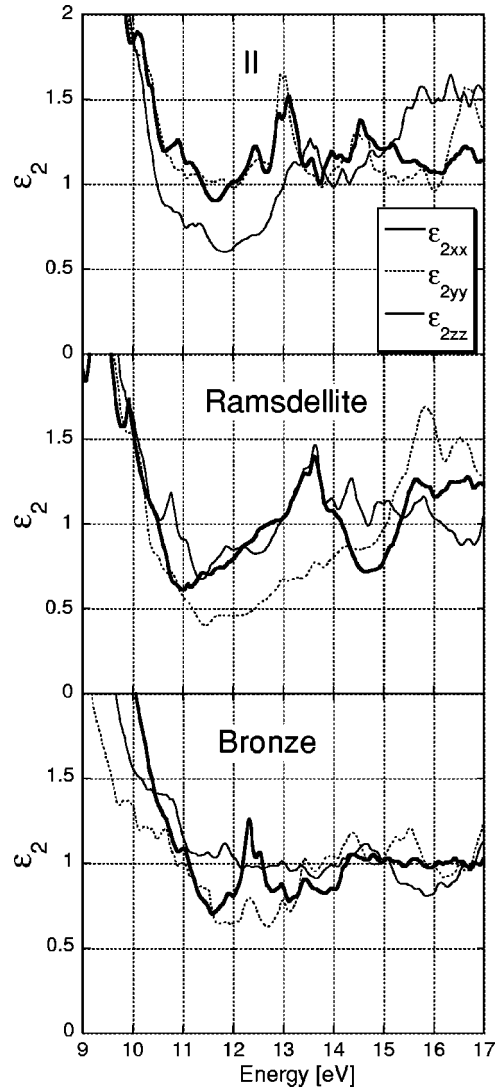


FIG. 11. Calculated imaginary parts of the dielectric function of Ramsdellite, II, and bronze TiO_2 structures.

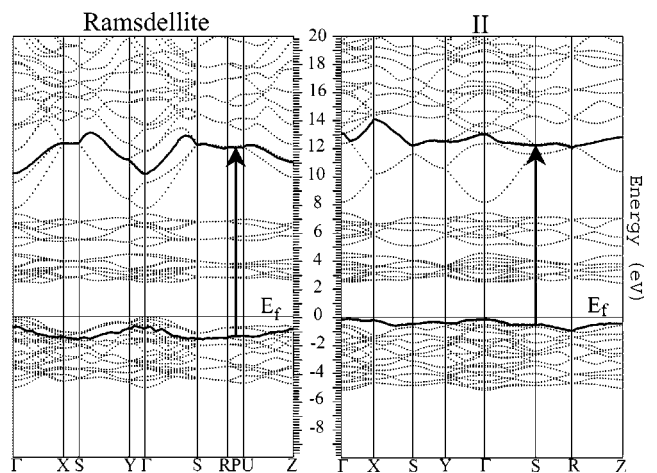


FIG. 12. Band structures of Ramsdellite and II TiO_2 . The bands involved in the RSU peak are thickened. An arrow indicates where the transition is the most intense (at the S and P points, respectively).

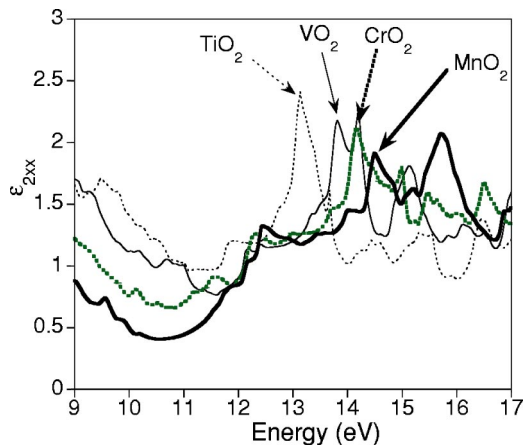


FIG. 13. Imaginary parts of the dielectric functions (excitation perpendicular to c axis) for the TiO_2 (dotted thin line), VO_2 (thin line), CrO_2 (dotted thick line), and MnO_2 (thick line) rutile phases. The RSU peak is indicated by an arrow for each phase.

Consequently, it is tempting to consider that the RSU peak could also be found in other oxides crystallizing in the rutile phase. To check on that assumption, calculations on other transition metal dioxides as well as 14th group element dioxides are presented below.

C. Other rutile oxides

Three other rutile phases involving atoms of the first row of transition metals are considered below. In Fig. 13, and following the same procedure as described earlier, we can identify a RSU peak in the ϵ_{2xx} of VO_2 , CrO_2 , and MnO_2 rutile phases. A progressive and monotonic shift of this peak is observed: 13.2 eV for TiO_2 , 13.8 eV for VO_2 , 14.2 eV for CrO_2 , and 14.5 eV for MnO_2 . This shift is due to the change of overlap of the metal $3d$ orbital with respect to the oxygen $2p$. Indeed, the larger the overlap integrals, the more (anti)bonding are the (anti)bonding levels created in the octahedron. The separation between the two levels is increased, and as ϵ_2 precisely measures the energy difference between these levels, a shift is observed. The interaction between the metal $3d$ levels and the oxygen $2p$ levels depends on the energy difference between these atomic levels as well as on the distances between the considered atoms. In going from left to right of the periodic table, the $3d$ levels go down in energy and get closer to the oxygen $2p$ levels. Equally, the mean M -O distances in the octahedra are 1.956 Å, 1.928 Å, 1.902 Å, and 1.888 Å for Ti, V, Cr, and Mn, respectively. Both criteria are met, which results in an increase of the overlap and, hence, of the transition energy. This is also confirmed by a comparison of the percentage of oxygen and M character at the A point as a function of M : 7–67%, 11–64%, 16–60%, 23–55% when going from Ti to Mn. The position of this peak is consequently related to the degree of covalence in the M and O bond.

The same conclusion can be achieved from the study of a series of rutile compounds with M originating from the same periodic table column. Figure 14 shows ϵ_{2xx} for SiO_2 , GeO_2 , SnO_2 , and PbO_2 in the rutile phase. The general fea-

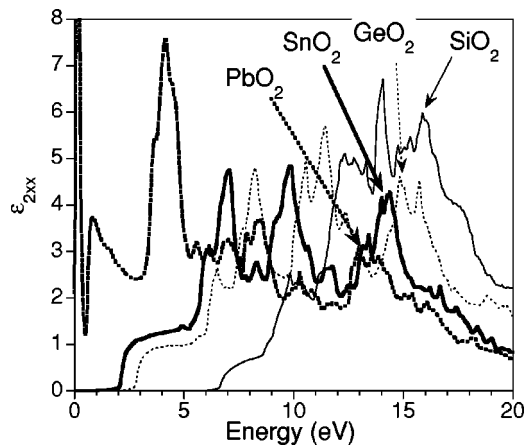


FIG. 14. Imaginary parts of the dielectric functions (excitation perpendicular to c axis) for the SiO_2 (thin line), GeO_2 (dotted thin line), SnO_2 (thick line), and PbO_2 (dotted thick line) rutile phases. The RSU peak is indicated by an arrow for each phase.

tures of the spectra are similar, with three main peaks after the intensity onset. For SiO_2 , GeO_2 , SnO_2 , and PbO_2 , the peak positions are 12.5–14–16 eV, 8.2–11.4–14.9 eV, 7.0–9.8–14.2 eV, and 4.2–8.4–13.5 eV, respectively. The study of the A \mathbf{k} point shows that the last peak is in fact related to RSUs and that the main interaction is between the M p levels and the oxygen $2p$ levels. The degree of overlap between these levels determines, as in the case of the transition metals, the direction and strength of the RSU peak position shift. It can be assessed by measuring the dispersion of the valence band in the band structures. This dispersion is 10.95 eV, 10.5 eV, 8.3 eV, and 8.3 eV for SiO_2 , GeO_2 , SnO_2 , and PbO_2 , respectively. The general trend is a decrease of the covalence from top to bottom of the 14th column leading to a decrease in the RSU peak energy. The interpretation is not as straightforward as that for transition metal compounds since the np levels are not the same (n is different) and the mean M -O distances vary considerably (1.774 Å, 1.884 Å, 2.054 Å, and 2.164 Å, from Si to Pb). This might explain the larger calculated shift for the characteristic peak ($\Delta E = 2.5$ eV) when compared to the transition metal series ($\Delta E = 1.3$ eV). Nevertheless, this shift is much smaller than the one observed for the other two peaks at 12.5 and 14 eV in SiO_2 ($\Delta E = 5.6$ and 9.8 eV, respectively). This is due to the fact that the states involved in the RSU peak are mainly made up of oxygen p orbitals. The robustness in the peak position as a function of M is consequently a striking particularity of the RSU peak.

V. CONCLUSION

We showed that low-energy loss spectra of rutile and anatase TiO_2 were different in the 10–15 eV region, due to the presence of a special transition around 14 eV. The precise analysis of this transition, thanks to *ab initio* band structure calculations, proves that it is due to states generated by Ti_3O_{15} rutile structural units. The existence and even the energy position of this transition can be generalized to other rutile phases in the first row of transition metals and in 14th column elements. Trends in the shift of this RSU peak as a

function of M can be related to the covalence of the M -O bond in a series.

It is believed that such characteristic peaks can be found in other materials and other structures. To a very large extent, it does not depend on the cation in the center of the octahedron. Fluorine rutile compounds are presently under investi-

gation to find out whether a characteristic peak also exists. A further development could be the study of perovskite structures: the identification of a characteristic peak in the corresponding low-energy loss spectra would make this technique as general as ELNES or EXELFS for structural determination.

- ¹T. Sikora, G. Hug, M. Jaouen, and J. J. Rehr, *Phys. Rev. B* **62**, 1723 (2000).
- ²D. H. Pearson, C. C. Ahn, and B. Fultz, *Phys. Rev. B* **47**, 8471 (1993).
- ³T. Hoche, P. Ohle, R. Keding, C. Russel, P. A. Van Aken, R. Schneider, H. J. Kleebe, X. Q. Wang, A. J. Jacobson, and S. Stemmer, *Philos. Mag.* **83**, 165 (2003).
- ⁴A. Gloter, V. Serin, C. Turquat, C. Cesari, C. Leroux, and G. Nihoul, *Eur. Phys. J. B* **22**, 179 (2001).
- ⁵A. C. Ferrari, A. Libassi, B. K. Tanner, V. Stolojan, J. Yuan, L. M. Brown, S. E. Rodil, B. Kleinsorge, and J. Robertson, *Phys. Rev. B* **62**, 11 089 (2000).
- ⁶J.-L. Mansot, V. Golabkan, L. Romana, and T. Césaire, *J. Microsc.* **210**, 110 (2003).
- ⁷P. Moreau, N. Brun, C. A. Walsh, C. Colliex, and A. Howie, *Phys. Rev. B* **56**, 6774 (1997).
- ⁸X. Liu, T. Pichler, M. Knupfer, and J. Fink, *Phys. Rev. B* **67**, 125403 (2003).
- ⁹L. Laffont, M. Monthieux, and V. Serin, *Carbon* **40**, 767 (2002).
- ¹⁰B. Rafferty and L. M. Brown, *Phys. Rev. B* **58**, 10 326 (1998).
- ¹¹A. Gutiérrez-Sosa, U. Bangert, A. J. Harvey, C. J. Fall, R. Jones, P. R. Briddon, and M. I. Heggie, *Phys. Rev. B* **66**, 035302 (2002).
- ¹²R. F. Egerton, *Electron Energy Loss Spectroscopy in the Electron Microscope*, 2nd ed. (Plenum Press, New York, 1996).
- ¹³M. Kadoshima, M. Hiratani, Y. Shimamoto, K. Torii, H. Miki, S. Kimura, and T. Nabatame, *Thin Solid Films* **424**, 224 (2003).
- ¹⁴P. A. Christensen, A. Dilks, T. A. Egerton, E. J. Lawson, and J. Temperley, *J. Mater. Sci.* **37**, 4901 (2002).
- ¹⁵K. Oyoshi, N. Sumi, I. Umezu, R. Souda, A. Yamazaki, H. Haneda, and T. Mitsuhashi, *Nucl. Instrum. Methods Phys. Res. B* **168**, 221 (2000).
- ¹⁶M. Grätzel, *Nature (London)* **414**, 338 (2001).
- ¹⁷R. K. B. Gover, J. R. Tolchard, H. Tukamoto, T. Murai, and J. T. S. Irvine, *J. Electrochem. Soc.* **146**, 4348 (1999).
- ¹⁸T. Chiamonte, L. P. Cardoso, R. V. Gelamo, F. Fabreguette, M. Sacilotti, M. C. Marco de Lucas, L. Imhoff, S. Bourgeois, Y. Kihn, and M.-J. Casanove, *Appl. Surf. Sci.* **212–213**, 661 (2003).
- ¹⁹G. Subramania, K. Constant, R. Biswas, M. M. Sigalas, and K.-M. Ho, *Appl. Phys. Lett.* **74**, 3933 (1999).
- ²⁰P. I. Sorantin and K. Schwarz, *Inorg. Chem.* **31**, 567 (1992).
- ²¹K. M. Glassford and J. R. Chelikowsky, *Phys. Rev. B* **46**, 1284 (1992).
- ²²S.-D. Mo and W. Y. Ching, *Phys. Rev. B* **51**, 13 023 (1995).
- ²³M. Arai, S. Kohiki, H. Yoshikawa, S. Fukushima, Y. Waseda, and M. Oku, *Phys. Rev. B* **65**, 085101 (2002).
- ²⁴N. Vast, L. Reining, V. Olevano, P. Schattschneider, and B. Jouffrey, *Phys. Rev. Lett.* **88**, 037601 (2002).
- ²⁵P. Fallon and C. A. Walsh, Computer code PEELS (University of Cambridge, England, 1996).
- ²⁶A. P. Stephens, Ph.D. thesis, University of Cambridge, Cambridge, England, 1980.
- ²⁷T. Malis, S. C. Chen, and R. F. Egerton, *J. Electron Microsc. Tech.* **8**, 193 (1988).
- ²⁸T. Stöckli, J.-M. Bonard, A. Châtelain, Z. L. Wang, and P. Stadelmann, *Phys. Rev. B* **61**, 5751 (2000).
- ²⁹P. Blaha, K. Schwarz, G. K. H. Madsen, D. Kvasnicka, and J. Luitz, Computer code WIEN2K (Technische Universität Wien, Austria, 2001).
- ³⁰P. Blaha, K. Schwarz, P. Sorantin, and S. B. Trickey, *Comput. Phys. Commun.* **59**, 399 (1990).
- ³¹J. P. Perdew and Y. Wang, *Phys. Rev. B* **45**, 13 244 (1992).
- ³²W. H. Baur, *Acta Crystallogr.* **14**, 493 (1961).
- ³³C. J. Howard, T. M. Sabine, and F. Dickson, *Acta Crystallogr., Sect. B: Struct. Sci.* **47**, 462 (1991).
- ³⁴I. E. Grey, C. Li, I. C. Madsen, and G. Braunschhausen, *Mater. Res. Bull.* **23**, 743 (1988).
- ³⁵T. P. Feist and P. K. Davies, *J. Solid State Chem.* **101**, 275 (1992).
- ³⁶J. Akimoto, Y. Gotoh, Y. Oosawa, N. Nonose, T. Kumagai, K. Aoki, and H. Takei, *J. Solid State Chem.* **113**, 27 (1994).
- ³⁷D. B. McWhan, M. Marezio, J. P. Remeika, and P. D. Dernier, *Phys. Rev. B* **10**, 490 (1974).
- ³⁸J. K. Burdett, G. J. Miller, J. W. Richardson Jr., and J. V. Smith, *J. Am. Chem. Soc.* **110**, 8064 (1988).
- ³⁹A. A. Bolzan, C. Fong, B. J. Kennedy, and C. J. Howard, *Aust. J. Chem.* **46**, 939 (1993).
- ⁴⁰W. H. Baur and A. A. Khan, *Acta Crystallogr., Sect. B: Struct. Crystallogr. Cryst. Chem.* **27**, 2133 (1971).
- ⁴¹A. A. Bolzan, C. Fong, B. J. Kennedy, and C. J. Howard, *Acta Crystallogr., Sect. B: Struct. Sci.* **53**, 373 (1997).
- ⁴²H. Seki, N. Ishizawa, N. Mizutani, and M. Kato, *J. Ceram. Assoc. Jpn.* **92**, 219 (1984).
- ⁴³H. Harada, Y. Sasa, and M. Uda, *J. Appl. Crystallogr.* **14**, 141 (1981).
- ⁴⁴C. Ambrosch-Draxl, J. A. Majewski, P. Vogl, and G. Leising, *Phys. Rev. B* **51**, 9668 (1995).
- ⁴⁵H. G. Wessjohann, *Z. Phys.* **269**, 269 (1974); *Phys. Status Solidi B* **77**, 535 (1976).
- ⁴⁶P. Moreau and M.-C. Cheynet, *Ultramicroscopy* **94**, 293 (2003).
- ⁴⁷L. A. Feldkamp, S. S. Shinozaki, C. A. Kukkonen, and S. P. Faile, *Phys. Rev. B* **19**, 2291 (1979).
- ⁴⁸J. Daniels, C. V. Festenberg, H. Raether, and K. Zeppenfeld, *Optical Constants of Solids by Electron Spectroscopy*, Vol. 54 of *Springer Tracts in Modern Physics* (Springer-Verlag, New York, 1970), pp. 78–135.
- ⁴⁹F. J. García de Abajo and A. Howie, *Phys. Rev. B* **65**, 115418 (2002).
- ⁵⁰P. Fallon, Computer code DK (University of Cambridge, England, 1991).